

Measurement of W-Pair Cross Sections in e^+e^- Interactions at $\sqrt{s} = 183$ GeV and W-Decay Branching Fractions

The L3 Collaboration

Abstract

We report on the measurement of W-boson pair-production with the L3 detector at LEP. In a data sample corresponding to a total luminosity of 55.47 pb^{-1} collected at an average centre-of-mass energy of 182.68 GeV, we select 824 four-fermion events with pairs of hadronic jets or pairs of leptons with high invariant masses. Branching fractions of W decays into different fermion-antifermion pairs are determined. Assuming charged-current lepton universality, the branching fraction for hadronic W decays is measured to be: $B(W \rightarrow \text{hadrons}) = 70.1 \pm 1.3 \text{ (stat.)} \pm 0.4 \text{ (syst.)} \%$. Combining all final states the total cross section for W-pair production is measured to be: $\sigma_{\text{WW}} = 16.53 \pm 0.67 \text{ (stat.)} \pm 0.26 \text{ (syst.) pb}$.

Submitted to *Phys. Lett. B*

1 Introduction

For the 1997 data taking period, the centre-of-mass energy, \sqrt{s} , of the e^+e^- collider LEP at CERN was increased to 183 GeV. This energy is well above the kinematic threshold of W-boson pair production, $e^+e^- \rightarrow W^+W^-$.

To lowest order within the Standard Model [1], three Feynman diagrams contribute to W-pair production, the s -channel γ and Z-boson exchange and the t -channel ν_e exchange, referred to as CC03 [2–4]. The W boson decays into a quark-antiquark pair, for example $W^- \rightarrow \bar{u}d$ or $\bar{c}s$, or a lepton-antilepton pair, $W^- \rightarrow \ell^-\bar{\nu}_\ell$ ($\ell = e, \mu, \tau$); in the following denoted as qq , $\ell\nu$ or ff in general for both W^+ and W^- decays. Additional contributions to the production of four-fermion final states arising from other neutral-current (NC) or charged-current (CC) Feynman diagrams are small. At the current level of statistical accuracy the interference effects need to be taken into account only for $e^+e^- \rightarrow \ell\nu\ell\nu(\gamma)$ (CC56+NC56) and $e^+e^- \rightarrow qqe\nu(\gamma)$ (CC20) [2–4].

During the 1997 run the L3 detector collected integrated luminosities of 4.04 pb^{-1} , 49.58 pb^{-1} and 1.85 pb^{-1} at centre-of-mass energies of 181.70 GeV, 182.72 GeV and 183.79 GeV, respectively, where these centre-of-mass energies are known to $\pm 0.05 \text{ GeV}$ [5]. For the results presented here these three data samples are combined for a total luminosity of 55.47 pb^{-1} and a luminosity weighted mean $\sqrt{s} = 182.68 \pm 0.05 \text{ GeV}$.

The cross section is measured for all four-fermion final states mediated by W-pair production. Combining these measurements W-decay branching fractions and the total W-pair production cross section are determined with significantly improved precision compared to earlier measurements with less luminosity reported by L3 [6] and other LEP experiments [7].

2 Analysis of Four-Fermion Production

The L3 detector is described in detail in Reference 8. The selections of the four-fermion final states are similar to the ones used at $\sqrt{s} = 161 \text{ GeV}$ and at $\sqrt{s} = 172 \text{ GeV}$. Charged leptons are explicitly identified using their characteristic signature. In general, electrons are identified as energy depositions in the BGO electromagnetic calorimeter with electromagnetic shower shape which are matched in azimuth to a track reconstructed in the central tracking chamber (TEC). Muons are identified either as tracks reconstructed in the muon chambers pointing back to the interaction vertex or by their minimum-ionising-particle (MIP) signature. Jets arising from hadronic τ decays are reconstructed based on a jet-clustering inside a cone of 15° half-opening angle [9]. Hadronic jets corresponding to quarks are reconstructed using the Durham jet algorithm [10] and adding four-momenta during the combination process. The momentum of the neutrino in $e^+e^- \rightarrow qq\ell\nu$ events is identified with the missing momentum vector.

Selection efficiencies and background contaminations of all processes are determined by Monte Carlo simulations. The following Monte Carlo event generators are used to simulate the various signal and background processes: KORALW [11] and HERWIG [12] ($e^+e^- \rightarrow WW \rightarrow ffff(\gamma)$); EXCALIBUR [13] ($e^+e^- \rightarrow ffff(\gamma)$); PYTHIA [14] ($e^+e^- \rightarrow q\bar{q}(\gamma), ZZ(\gamma)$); KORALZ [15] ($e^+e^- \rightarrow \mu^+\mu^-(\gamma), \tau^+\tau^-(\gamma)$); BHAGENE3 [16], BHWIDE [17] and TEEGG [18] ($e^+e^- \rightarrow e^+e^-(\gamma)$), DIAG36 [19] and LEP4F [20] (leptonic two-photon collisions); PHOJET [21] (hadronic two-photon collisions). The response of the L3 detector is modelled with the GEANT [22] detector simulation program which includes the effects of energy loss, multiple scattering and showering in the detector materials and in the beam pipe.

Systematic uncertainties due to Bose Einstein correlations, colour reconnection effects and fragmentation models are estimated by comparing different Monte Carlo programs to simulate

the signal. Uncertainties in the description of initial- and final state radiation are estimated by determining efficiencies also for events containing soft radiative photons only. Differences are small and half of the observed effects are taken as systematic errors. The dependence of the selection efficiencies on mass and total width of the W boson and the effect of diagrams beyond CC03 are studied with improved statistical accuracy by reweighting Monte Carlo events [23]. The measurement of the total luminosity, \mathcal{L} , follows the procedure described in Reference 24. The total error on the luminosity measurement for the 1997 data is estimated to be 0.3%.

The results on cross sections and W-decay branching fractions are determined in a combined analysis taking migration between the various final states into account [6]. The results are compared to the predictions of the Standard Model calculated for a mass of the W boson of $M_W = 80.33$ GeV [25] using the GENTLE [26] program.

2.1 $e^+e^- \rightarrow \ell\nu\ell\nu(\gamma)$

The event selection for the process $e^+e^- \rightarrow \ell\nu\ell\nu(\gamma)$ requires two charged leptons and missing energy due to the neutrinos. Low-multiplicity leptonic final states are selected by requiring between one and six TEC tracks and between one and 15 calorimetric clusters. The visible energy of the event is required to be larger than 2% and smaller than 80% of \sqrt{s} .

The selection depends on whether the event contains zero, one or two identified electrons or muons, referred to as jet-jet, lepton-jet and lepton-lepton class. Electrons, muons and τ jets are identified inside the polar angular range of $|\cos\theta| < 0.96$. For events with one or two electrons, one electron should lie in the angular range $|\cos\theta| < 0.92$ in order to limit the amount of background from Bhabha scattering. For events containing jets only, the two highest energy jets must also satisfy $|\cos\theta| < 0.92$.

In the lepton-lepton class, the energy of the two leptons must be larger than 20 GeV and 5 GeV, respectively, and smaller than 80 GeV. In order to reject $\ell^+\ell^-(\gamma)$ events, the acoplanarity between the two leptons is required to be larger than 8° . Exactly two TEC tracks must be reconstructed. The transverse energy imbalance must be at least 8 GeV and larger than 10% of the visible energy. The calorimetric energy not associated with the two leptons is required to be less than 10 GeV.

In the lepton-jet class, the energy of the electron or muon must be larger than 10 GeV and smaller than 80 GeV. In addition a jet with more than 8 GeV energy is required. The acoplanarity between the lepton and the jet as well as between the lepton and any TEC track must be larger than 8° . At least one TEC track must have a momentum larger than 2 GeV. The missing transverse energy must exceed 10% of the visible energy and, in order to reject radiative $\ell^+\ell^-(\gamma)$ events where the photon escapes along the beam pipe, the polar angle of the missing momentum vector must satisfy $|\cos\theta_{miss}| < 0.98$. For muons identified by their MIP signature the missing energy vector is required to point at least 23° in polar angle away from the MIP muon. Events containing photons with an energy of more than 10 GeV are rejected.

In the jet-jet class, events with two or three jets are accepted. The energy of at least two jets must be larger than 10 GeV and 6 GeV, respectively. The missing transverse energy must exceed 10% of the visible energy, and the polar angle of the missing momentum vector must satisfy $|\cos\theta_{miss}| < 0.98$. At least two TEC tracks with momentum above 5 GeV and 1 GeV, respectively, are required. Both jets must be accompanied by at least one TEC track within 11.5° in azimuth. The sum of the energy of reconstructed photons must not exceed 50 GeV, and the energy measured in the angular region $|\cos\theta| > 0.98$ must be smaller than 20 GeV. The smallest acoplanarity angle between any two TEC tracks must be larger than 14° .

A cosmic ray rejection is applied for all three event classes, based on the radial distance of closest approach of the muon to the beam line, a match in polar and azimuthal angle of a TEC track with the track reconstructed in the muon chambers, and scintillator time measurements.

A total of 54 events is selected in the data: 26 lepton-lepton events, 25 lepton-jet events and 3 jet-jet events. The distributions of the acoplanarity between the two charged leptons and of the lepton energy for lepton-lepton and lepton-jet events are shown in Figure 1.

The signal efficiencies are determined from CC56+NC56 Monte Carlo samples within the following phase-space cuts: $|\cos\theta| < 0.96$ for both charged leptons, with energies larger than 15 GeV and 5 GeV, respectively. Efficiencies are given in the form of a 6 by 6 matrix, as shown in Table 1, relating $\ell\nu\ell\nu$ events at four-fermion level to $\ell\nu\ell\nu$ events at reconstruction level. The background contributions are listed in Table 2.

The dominant contribution to the systematic error on the measured cross section arises from the limited statistics of Monte Carlo simulations for the background processes. Uncertainties due to an imperfect detector description by the Monte Carlo simulation are dominated by the uncertainty in the energy scale of the calorimeters. All contributions to the systematic error are listed in Table 3. A total systematic error of 3.3% on the measured cross section is obtained.

2.2 $e^+e^- \rightarrow qqe\nu(\gamma)$

The event selection for the process $e^+e^- \rightarrow qqe\nu(\gamma)$ requires an identified electron of at least 20 GeV, high particle multiplicity arising from the $q\bar{q}$ system, and missing momentum due to the neutrino. In addition, electrons are also identified in the lead scintillator calorimeter, SPACAL, located between the BGO barrel and endcap, as the highest energy deposition with less than 0.2 GeV energy deposited in the hadron calorimeter directly behind the SPACAL cluster.

Electrons arising from the decays of hadrons are rejected by requiring the electron to be isolated from the hadronic system. For electron candidates in the BGO, the electron energy must account for at least 73% of the total calorimetric energy deposited in a cone of half-opening angle 15° around the electron direction. For SPACAL electrons, the energy in the hadron calorimeter in a cone of 7° half-opening angle must be less than 8 GeV.

For the selection of events with the electron candidate identified in the BGO (SPACAL), the same selection variables are used. Purely leptonic final states are rejected by requiring at least 12 (17) calorimetric clusters. After having removed the track and calorimetric energy depositions associated to the identified electron, the remainder of the event is grouped into two hadronic jets. The invariant mass of the jet-jet system must be larger than 33 (48) GeV. The invariant mass of the electron-neutrino system must be larger than 60 (60) GeV in order to reject $e^+e^- \rightarrow qq\tau\nu(\gamma)$ events.

A TEC track must match the electron candidate within $\pm 2.3^\circ$ ($\pm 5.7^\circ$) in azimuth in order to reject radiative photons. Converted photons are rejected by requiring the difference of the electron energy measured in the electromagnetic calorimeter and the momentum of the associated track to be less than 61 (38) GeV. For electron candidates at low polar angles, $|\cos\theta_e| > 0.9$, the requirement of a matched track is replaced by the requirement that the solid angle subtended by the directions of the two hadronic jets and the electron must be smaller than 5.4 sr, rejecting $e^+e^- \rightarrow q\bar{q}(\gamma)$ events which are planar. In order to reject radiative $q\bar{q}(\gamma)$ events where the photon escapes along the beam pipe, the polar angle of the missing momentum vector must point inside the detector, $|\cos\theta_\nu| < 0.94$ (0.91). Any muon is required to have a transverse momentum with respect to the nearest jet of less than 17 GeV (14 GeV).

A total of 112 events is selected in the data: 110 events with the electron identified in the BGO electromagnetic calorimeter and two events with the electron identified in the SPACAL calorimeter. The distributions of the polar angle of the neutrino and of the neutrino-electron invariant mass are shown in Figure 2.

The signal efficiency is determined from a CC20 Monte Carlo sample within the following phase-space cuts: $E_e, E_\nu > 20$ GeV; $|\cos \theta_e|, |\cos \theta_\nu| < 0.95$; $M_{e\nu}, M_{qq} > 45$ GeV. The selection efficiencies and the background contributions are listed in Tables 1 and 2.

The systematic error on the measured cross section arising from the selection is obtained by varying the cut position around the nominal value. Systematic errors due to mismatch between data and Monte Carlo are studied by using control samples of $e^+e^- \rightarrow q\bar{q}(\gamma)$ events and varying the energy scale and resolution of jets. Uncertainties in the accepted background cross sections are estimated by comparing different Monte Carlo programs to simulate the background. All contributions to the systematic error are listed in Table 3. A total systematic error of 1.7% on the measured cross section is obtained.

2.3 $e^+e^- \rightarrow qq\mu\nu(\gamma)$

The event selection for the process $e^+e^- \rightarrow qq\mu\nu(\gamma)$ requires high particle multiplicity arising from the $q\bar{q}$ system, an identified muon and missing momentum due to the neutrino. Events must contain more than ten calorimetric clusters and more than five TEC tracks in order to reject purely leptonic final states as well as cosmic-ray background. Removing the track and energy depositions associated to the identified muon, the remaining event is clustered to form two hadronic jets. The invariant mass of the system of two hadronic jets must lie between 20 GeV and 120 GeV.

Muons identified in the muon spectrometer must have a momentum larger than 15 GeV. The energy deposited in the calorimeters in a cone of 15° half-opening angle around the muon must be less than 20 GeV in order to reject muons from the decay of hadrons. The muon-neutrino invariant mass, $M_{\mu\nu}$, must be larger than 45 GeV, rejecting $e^+e^- \rightarrow qq\tau\nu(\gamma)$ events. The TEC track associated to the MIP must point back to the interaction vertex and have a momentum larger than 20 GeV. The energy deposited in the BGO electromagnetic calorimeter associated to the MIP must lie between 0.2 GeV and 2 GeV. The energy deposited in the calorimeters in a cone of 15° half-opening angle around the MIP muon must be less than 7 GeV. The inclusion of MIP based muon identification increases the efficiency by 11% relative.

The background of $e^+e^- \rightarrow q\bar{q}(\gamma)$ events with inclusive muons and missing energy along the beam pipe due to initial-state photon radiation is further reduced by requiring the product $\alpha \sin \theta_\nu$ to be larger than 4° , where θ_ν is the polar angle of the missing momentum vector and α is the angle of the muon to the nearest of the two hadronic jets.

A total of 108 events is selected in the data: 96 events with a muon reconstructed in the muon spectrometer and 12 events with a muon identified by its MIP signature. The distributions of the muon momentum and of the quantity $\alpha \sin \theta_\nu$ are shown in Figure 3. The selection efficiencies and background contribution are listed in Tables 1 and 2.

Systematic errors in the muon identification are derived from a comparison of data versus Monte Carlo using $e^+e^- \rightarrow \mu^+\mu^-(\gamma)$ events collected at $\sqrt{s} = 91$ GeV and 183 GeV. The dominant contribution is the uncertainty in the efficiency of the muon chambers. Control samples of $e^+e^- \rightarrow q\bar{q}(\gamma)$ are used to estimate uncertainties in jet energy scale and resolution. All contributions to the systematic error are listed in Table 3. A total systematic error of 1.7% on the measured cross section is obtained.

2.4 $e^+e^- \rightarrow qq\tau\nu(\gamma)$

The event selection for the process $e^+e^- \rightarrow qq\tau\nu(\gamma)$ is based on the identification of a tau jet in a hadronic event with missing energy. Events must have more than 14 calorimetric clusters and more than five TEC tracks in order to reject low-multiplicity leptonic final states. Signal events contain at least two neutrinos, resulting in missing momentum and reduced visible energy. In order to reject $e^+e^- \rightarrow q\bar{q}(\gamma)$, $qqqq(\gamma)$ events the difference between the visible energy and the missing momentum must be less than 140 GeV, the sum of the missing momentum and visible mass must be greater than 110 GeV and the transverse energy imbalance must be larger than 10 GeV. Requiring the longitudinal energy imbalance to be smaller than 40 GeV suppresses $e^+e^- \rightarrow q\bar{q}(\gamma)$ events with hard initial-state radiation.

In events with the τ decaying into an electron or muon, the energy of that lepton must be larger than 5 GeV. The invariant mass of the system of the lepton, electron or muon, and the neutrino must be less than 60 GeV and 45 GeV in order to reject $e^+e^- \rightarrow qqe\nu(\gamma)$ and $e^+e^- \rightarrow qq\mu\nu(\gamma)$ events, respectively.

If no electrons or muons are found, jets are reconstructed based on clustering inside a cone of 15° half-opening angle [9]. At least three reconstructed jets are required. The hadronically decaying τ is identified among the three jets of highest energy using a neural network based on five input variables: the number of TEC tracks and calorimetric clusters associated to the jet, the half-opening angle of the jet, its electromagnetic energy and its mass. The jet with the highest output value of the neural network is considered as the τ jet candidate with a probability of misidentification less than 20%.

If the energy of the τ jet is below 10 GeV the τ jet is required to have an angular separation of at least 37° to the nearest jet. The identified τ jet must contain between one and three TEC tracks. The polar angle of the missing momentum vector, θ_{miss} , must satisfy $|\cos \theta_{miss}| < 0.95$ to further reduce the $e^+e^- \rightarrow q\bar{q}(\gamma)$ background. For events with a transverse energy imbalance less than 20 GeV and with $|\cos \theta_{miss}| > 0.55$, a loose cut on the output of the neural network is applied.

In order to reduce the background from $e^+e^- \rightarrow qqe\nu(\gamma)$ events where the electron is not identified, events with the τ jet having more than 35 GeV of energy deposited in the electromagnetic calorimeter and less than 2 GeV in the hadronic calorimeter are rejected. For one-track τ jets in the SPACAL region, where the electron rejection is less efficient, either the hadronic energy of the τ jet must be larger than 5 GeV or the momentum of the associated TEC track must be smaller than 20 GeV. The background of $e^+e^- \rightarrow qq\mu\nu(\gamma)$ events where the muon is not identified in the muon chambers is reduced by rejecting events where the τ jet is compatible with a MIP.

After having removed the tracks and calorimetric energy depositions associated with the identified τ jet, the remaining tracks and calorimetric clusters are grouped into two hadronic jets using the Durham jet algorithm. The invariant mass of the jet-jet system must be larger than 50 GeV and smaller than 110 GeV. The system of the τ jet and the missing four-momentum must have an invariant mass larger than 40 GeV and smaller than 120 GeV.

A total of 77 events is selected in the data: 9 $\tau \rightarrow \nu e\bar{\nu}$ events, 9 $\tau \rightarrow \nu\mu\bar{\nu}$ events and 59 $\tau \rightarrow \nu$ hadrons events. The distributions of the number of TEC tracks associated to the τ jet and of the invariant mass of the $q\bar{q}$ system are shown in Figure 4. The selection efficiencies and the background contributions are listed in Tables 1 and 2.

Systematic errors affecting the $e^+e^- \rightarrow qq\tau\nu(\gamma)$ selection are derived from a comparison of data and Monte Carlo simulation based on high-statistics $e^+e^- \rightarrow q\bar{q}(\gamma)$ and $e^+e^- \rightarrow \tau^+\tau^-(\gamma)$ event samples collected at $\sqrt{s} = 91$ GeV. A τ jet from a $\tau^+\tau^-(\gamma)$ event is combined with a

$q\bar{q}(\gamma)$ event. Selection quantities are also studied on these mixed events. All contributions to the systematic error are listed in Table 3. A total systematic error of 3.3% on the measured cross section is obtained.

2.5 $e^+e^- \rightarrow qqqq(\gamma)$

High multiplicity events are selected by requiring at least ten TEC tracks and at least 30 calorimetric clusters. Events must have a visible energy, E_{vis} , larger than $0.7\sqrt{s}$ and a longitudinal energy imbalance less than $0.25E_{\text{vis}}$. Tracks and calorimetric clusters are grouped into four jets. The Durham jet-resolution parameter at which the event changes from a four-jet to a three-jet topology, Y_{34} , must be larger than 0.0015 to enhance the four-jet signal. To suppress $e^+e^- \rightarrow q\bar{q}(\gamma)$ background with hard radiative photons recorded in the detector, an event is rejected if it contains an electromagnetic cluster with an energy of more than 40 GeV, or if more than 80% of the energy of any jet is attributed to the most energetic photon. Events containing muons reconstructed in the muon chambers with more than 25 GeV are rejected.

The selection accepts 95.6% of the $WW \rightarrow qqqq(\gamma)$ signal while reducing the dominating $e^+e^- \rightarrow q\bar{q}(\gamma)$ background by a factor of 15. A total of 864 events passes the selection. The determination of jet energies and angles is improved by a kinematic fit imposing four-momentum conservation. Two pairs of jets are formed, corresponding to two W bosons, with invariant masses M_1 and M_2 . Of all combinations, the optimal pairing of jets is that with the smallest mass difference, $|M_1 - M_2|$, disregarding the jet-jet pairing yielding the smallest mass sum, $M_1 + M_2$. This algorithm yields the correct assignment of jets to W bosons for 74% of the selected signal events.

A neural network is trained to separate the signal from the dominating $e^+e^- \rightarrow q\bar{q}(\gamma)$ background. The input to the network consists of eight variables: minimal and maximal jet energy, minimal jet-jet opening angle, minimal jet cluster multiplicity, Y_{34} , sphericity, difference of the two W masses and average mass of two jets when the event is reconstructed as a two jet event. The distributions of the maximal jet energy, the minimal jet-jet angle, average jet mass when the event is reconstructed as a two jet event, and the difference of the two W masses are shown in Figure 5. The network is trained such that the output peaks at one for the signal and at zero for the background. The distribution of the neural-network output is shown in Figure 6.

The neural-network output distribution for data events is fitted by a linear combination of neural-network output distributions derived from Monte Carlo simulations for signal and background [6]. The results of the fit correspond to a signal cross section of 8.35 ± 0.46 pb and a $e^+e^- \rightarrow q\bar{q}(\gamma)$ cross section of 105 ± 6 pb where the errors are statistical. The measured $e^+e^- \rightarrow q\bar{q}(\gamma)$ cross section is in good agreement with both our dedicated measurements of fermion-pair cross sections and with the Standard Model value.

As a cross check the signal cross section is determined by applying a cut on the output of the neural network larger than 0.67, which minimises the expected statistical error. The selection efficiencies and the background contributions corresponding to this cut are listed in Tables 1 and 2. A total of 473 events is selected in the data, yielding a signal cross section of 8.01 ± 0.45 pb. The high signal cross section obtained by the fit arises due to the large number of data events with very high neural-network output. Other analyses using cut-based selections or event weighting methods yield consistent results.

The systematic error on the measured cross section due to a discrepancy in the four-jet event rate between the $e^+e^- \rightarrow q\bar{q}(\gamma)$ data and the Monte Carlo is estimated by reweighting $q\bar{q}(\gamma)$ Monte Carlo events as a function of Y_{34} . The reweighting function is derived from a

comparison between data and Monte Carlo of hadronic Z decays collected at $\sqrt{s} = 91$ GeV. The systematic uncertainty of the selection is dominated by the imperfect simulation of the jet cluster multiplicity. A total systematic error of 2.7% on the measured cross section is obtained.

3 Results

The cross sections, σ_i , of the signal processes i are determined simultaneously in one maximum-likelihood fit, taking cross feed between final states into account. The fitting procedure to determine cross sections of the signal processes, W-decay branching fractions and the total W-pair cross section is identical to the one used previously [6].

For the purely leptonic final states the fitting procedure determines six different cross sections corresponding to all possible combinations of flavours of the two final-state lepton pairs. Since the data statistics for the $\ell\nu\ell\nu(\gamma)$ final state is low, the sum of these six cross sections is quoted as the cross section for the process $e^+e^- \rightarrow \ell\nu\ell\nu(\gamma)$.

3.1 Signal Cross Sections

For the $qqe\nu(\gamma)$ and the six $\ell\nu\ell\nu(\gamma)$ final states the cross sections are determined within phase-space cuts to reduce contributions from processes not mediated by resonant W-pair production. In order to determine W-pair cross sections for these final states the measured cross sections are scaled by a multiplicative factor, f_i , as listed in Table 2. The conversion factors f_i are given by the ratio of the total CC03 cross section and the four-fermion cross section within phase-space cuts, and are calculated within the Standard Model using EXCALIBUR.

The resulting cross sections including statistical and systematic errors are listed in Table 4. The Standard Model agrees well with these results. Since the efficiency matrix of Table 1 contains non-zero off-diagonal elements, the five cross sections are correlated. The largest correlations, -11% and -16% , arise among the semileptonic channels between $qq\tau\nu$ and $qqe\nu$ and between $qq\tau\nu$ and $qq\mu\nu$. All other correlations are smaller than 1% in magnitude and thus negligible.

3.2 W-Decay Branching Fractions and W-Pair Cross Section

For the determination of the total CC03 production cross section of W-pairs, σ_{WW} , the signal cross sections σ_i are replaced by the product $r_i\sigma_{\text{WW}}$ or $r_i\sigma_{\text{WW}}/f_i$ for the $qqe\nu(\gamma)$ and $\ell\nu\ell\nu(\gamma)$ final states. The ratios r_i are given in terms of the W-decay branching fractions, $B(W \rightarrow qq)$ and $B(W \rightarrow \ell\nu)$, as follows: $r_{qqqq} = [B(W \rightarrow qq)]^2$, $r_{qq\ell\nu} = 2B(W \rightarrow qq)B(W \rightarrow \ell\nu)$, and $r_{\ell\nu\ell\nu} = [B(W \rightarrow \ell\nu)]^2$ for identical and $r_{\ell\nu\ell'\nu'} = 2B(W \rightarrow \ell\nu)B(W \rightarrow \ell'\nu')$ for different lepton flavours in the final state. The sum of the hadronic and the three leptonic branching fractions is constrained to be unity. For the determination of W-decay branching fractions the data collected at $\sqrt{s} = 161$ GeV and at $\sqrt{s} = 172$ GeV are included.

The resulting total W-pair cross section and the W-decay branching fractions including statistical and systematic errors and correlations are listed in Table 5. The branching fractions are determined both with and without the assumption of charged-current lepton universality in W decays. The W-decay branching fractions obtained for the individual leptons are in good agreement with each other and support this assumption. Assuming lepton universality, W-decay branching fraction and the W-pair cross sections are:

$$\sigma_{\ell\nu\ell\nu} = 1.47 \pm 0.24 \pm 0.05 \text{ pb} \quad \sigma_{qq\ell\nu} = 6.63 \pm 0.42 \pm 0.09 \text{ pb} \quad (1)$$

$$B(W \rightarrow qq) = 70.1 \pm 1.3 \pm 0.4 \%, \quad (2)$$

where the first error is statistical and the second systematic. The accuracy on the W-decay branching fractions is improved by about a factor of three with respect to our previous publication based on the 1996 data [6].

The branching fractions of the W boson depend on the six elements V_{ij} of the Cabibbo-Kobayashi-Maskawa quark mixing matrix V_{CKM} [27] not involving the top quark [3], $1/B(W \rightarrow \ell\nu) = 3 + 3[1 + \alpha_s(M_W)/\pi]V^2$, where α_s is the strong coupling constant. Our measurements correspond to:

$$V^2 = \sum_{i=u,c; j=d,s,b} |V_{ij}|^2 = 2.26 \pm 0.14 \pm 0.05. \quad (3)$$

The sensitivity of this measurement to a single matrix element is largest for the dominant diagonal elements of V_{CKM} . Since V_{ud} is known much more precisely than V_{cs} , it is most useful to determine the latter. Using the current world-average values and errors of the other matrix elements not assuming the unitarity of V_{CKM} [28], the result is:

$$|V_{cs}| = 1.10 \pm 0.06 \pm 0.02. \quad (4)$$

The statistical error includes the errors on α_s and the other V_{ij} but is dominated by the statistical error on the W branching fractions.

The W-pair cross section is also derived imposing the W-decay branching fractions as expected within the Standard Model [3]. The result for the total production cross section of W-pairs at $\sqrt{s} = 182.68 \pm 0.05$ GeV is:

$$\sigma_{\text{WW}} = 16.53 \pm 0.67 \pm 0.26 \text{ pb}. \quad (5)$$

Our published measurements of σ_{WW} at $\sqrt{s} = 161$ GeV, at $\sqrt{s} = 172$ GeV and the new result at $\sqrt{s} = 183$ GeV presented here are compared to the Standard Model expectation in Figure 7. The deviation from pure t -channel ν_e exchange in W-pair production is clearly visible. Both non-Abelian s -channel diagrams with triple-gauge-boson couplings as expected within the Standard Model are needed to obtain agreement with our measurements.

The cross section for W-pair production depends both on the total decay width of the W boson, $\Gamma_{\text{W}}^{\text{tot}}$, appearing in the propagator, and on the partial decay widths of the W decay modes analysed. Allowing for additional undetected decay modes of the W boson, for example into massive weakly interacting neutral particles and very soft charged particles, the resulting invisible decay width, $\Gamma_{\text{W}}^{\text{inv}}$, enlarges the total width of the W boson, $\Gamma_{\text{W}}^{\text{tot}} = \Gamma_{\text{W}}^{\text{SM}} + \Gamma_{\text{W}}^{\text{inv}}$, where $\Gamma_{\text{W}}^{\text{SM}}$ is the visible W width as calculated in the Standard Model. Thus $\Gamma_{\text{W}}^{\text{inv}}$ is constrained by our cross section measurements. W-pair events where at least one W boson decays invisibly are assumed not to pass the above selections. Using the Standard Model relation to calculate the visible width, $\Gamma_{\text{W}}^{\text{SM}} = \Gamma_{\text{W}}^{\text{SM}}(M_{\text{W}})$ [3], the invisible width is determined to be $\Gamma_{\text{W}}^{\text{inv}} = -30 \pm 41$ MeV or $\Gamma_{\text{W}}^{\text{inv}} < 63$ MeV at 95% confidence level.

4 Acknowledgements

We wish to congratulate the CERN accelerator divisions for the successful upgrade of the LEP machine and to express our gratitude for its good performance. We acknowledge with appreciation the effort of all engineers, technicians and support staff who have participated in the construction and maintenance of this experiment.

References

- [1] S. L. Glashow, Nucl. Phys. **22** (1961) 579;
S. Weinberg, Phys. Rev. Lett. **19** (1967) 1264;
A. Salam, in *Elementary Particle Theory*, ed. N. Svartholm, Stockholm, Almquist and Wiksell (1968), 367.
- [2] D. Bardin *et al.*, Nucl. Phys. (Proc. Suppl.) **B 37** (1994) 148;
F.A. Berends *et al.*, Nucl. Phys. (Proc. Suppl.) **B 37** (1994) 163.
- [3] W. Beenakker *et al.*, in *Physics at LEP 2*, Report CERN 96-01 (1996), eds G. Altarelli, T. Sjöstrand, F. Zwirner, Vol. 1, p. 79.
- [4] D. Bardin *et al.*, in *Physics at LEP 2*, Report CERN 96-01 (1996), eds G. Altarelli, T. Sjöstrand, F. Zwirner, Vol. 2, p. 3.
- [5] The LEP Energy Working Group, *LEP energy calibration above the W pair production threshold*, LEP ECAL/98-02, ICHEP-98/352.
- [6] The L3 Collaboration, M. Acciarri *et al.*, Phys. Lett. **B 398** (1997) 223, Phys. Lett. **B 407** (1997) 419.
- [7] The ALEPH Collaboration, R. Barate *et al.*, Phys. Lett. **B 401** (1997) 347, Phys. Lett. **B 415** (1997) 435;
The DELPHI Collaboration, P. Abreu *et al.*, Phys. Lett. **B 397** (1997) 158, Euro. Phys. Jour. **C 2** (1998) 581;
The OPAL Collaboration, K. Ackerstaff *et al.*, Phys. Lett. **B 389** (1996) 416, Euro. Phys. Jour. **C 1** (1998) 425.
- [8] The L3 Collaboration, B. Adeva *et al.*, Nucl. Instr. and Meth. **A 289** (1990) 35;
M. Chemarin *et al.*, Nucl. Instr. and Meth. **A 349** (1994) 345;
M. Acciarri *et al.*, Nucl. Instr. and Meth. **A 351** (1994) 300;
G. Basti *et al.*, Nucl. Instr. and Meth. **A 374** (1996) 293;
I.C. Brock *et al.*, Nucl. Instr. and Meth. **A 381** (1996) 236;
A. Adam *et al.*, Nucl. Instr. and Meth. **A 383** (1996) 342.
- [9] H.J. Daum *et al.*, Z. Phys. **C 8** (1981) 167.
- [10] S. Catani *et al.*, Phys. Lett. **B 269** (1991) 432;
S. Bethke *et al.*, Nucl. Phys. **B 370** (1992) 310.
- [11] KORALW version 1.33 is used.
M. Skrzypek, S. Jadach, W. Placzek and Z. Wąs, Comp. Phys. Comm. **94** (1996) 216;
M. Skrzypek, S. Jadach, M. Martinez, W. Placzek and Z. Wąs, Phys. Lett. **B 372** (1996) 289.
- [12] HERWIG version 5.9 is used.
G. Marchesini and B. Webber, Nucl. Phys. **B 310** (1988) 461;
I.G. Knowles, Nucl. Phys. **B 310** (1988) 571;
G. Marchesini *et al.*, Comp. Phys. Comm. **67** (1992) 465.

- [13] F.A. Berends, R. Kleiss and R. Pittau, Nucl. Phys. **B 424** (1994) 308; Nucl. Phys. **B 426** (1994) 344; Nucl. Phys. (Proc. Suppl.) **B 37** (1994) 163;
R. Kleiss and R. Pittau, Comp. Phys. Comm. **83** (1994) 141;
R. Pittau, Phys. Lett. **B 335** (1994) 490.
- [14] PYTHIA version 5.722 is used.
T. Sjöstrand, *PYTHIA 5.7 and JETSET 7.4 Physics and Manual*,
CERN-TH/7112/93 (1993), revised August 1995; Comp. Phys. Comm. **82** (1994) 74.
- [15] KORALZ version 4.02 is used.
S. Jadach, B. F. L. Ward and Z. Wąs, Comp. Phys. Comm. **79** (1994) 503.
- [16] J.H. Field, Phys. Lett. **B 323** (1994) 432;
J.H. Field and T. Riemann, Comp. Phys. Comm. **94** (1996) 53.
- [17] BHWIDE version 1.01 is used.
S. Jadach, W. Placzek, B.F.L. Ward, Phys. Rev. **D 40** (1989) 3582, Comp. Phys. Comm. **70** (1992) 305, Preprint UTHEP-95-1001, hep-ph/9608412.
- [18] D. Karlen, Nucl. Phys. **B 289** (1987) 23.
- [19] F. A. Berends, P. H. Daverfeldt and R. Kleiss, Nucl. Phys. **B 253** (1985) 441.
- [20] J.A.M. Vermaseren, J. Smith and G. Grammer Jr, Phys. Rev. D **19** (1979) 137;
J.A.M. Vermaseren, Nucl. Phys. B **229** (1983) 347.
- [21] PHOJET version 1.05 is used.
R. Engel, Z. Phys. **C 66** (1995) 203; R. Engel and J. Ranft, Phys. Rev. **D 54** (1996) 4244.
- [22] The L3 detector simulation is based on GEANT Version 3.15.
R. Brun *et al.*, *GEANT 3*, CERN-DD/EE/84-1 (Revised), 1987.
The GHEISHA program (H. Fesefeldt, RWTH Aachen Report PITHA 85/02 (1985))
is used to simulate hadronic interactions.
- [23] The L3 Collaboration, M. Acciarri *et al.*, Phys. Lett. **B 413** (1997) 176.
- [24] The L3 Collaboration, I.C. Brock *et al.*, Nucl. Instr. and Meth. **A 381** (1996) 236.
- [25] The UA1 Collaboration, C. Albajar *et al.*, Z. Phys. **C 44** (1989) 15;
The UA2 Collaboration, J. Alitti *et al.*, Phys. Lett. **B 241** (1990) 150; Phys. Lett. **B 276** (1992) 354;
The CDF Collaboration, F. Abe *et al.*, Phys. Rev. Lett. **65** (1990) 2243; Phys. Rev. **D 43** (1991) 2070; Phys. Rev. Lett. **75** (1995) 11; Phys. Rev. **D 52** (1995) 4784;
The DØ Collaboration, S. Abachi *et al.*, Phys. Rev. Lett. **77** (1996) 3309.
We use the average value and error for the mass of the W boson as listed in:
R.M. Barnett *et al.*, *Review of Particle Properties*, Phys. Rev. **D 54** (1996) 1.
- [26] GENTLE version 2.0 is used. D. Bardin *et al.*, Comp. Phys. Comm. **104** (1997) 161.
- [27] N. Cabibbo, Phys. Rev. Lett. **10** (1963) 531;
M. Kobayashi and T. Maskawa, Prog. Theor. Phys. **49** (1973) 652.
- [28] C. Caso *et al.*, *The 1998 Review of Particle Physics*, Euro. Phys. Jour. **C 3** (1998) 1.

The L3 Collaboration:

M. Acciarri,²⁸ O. Adriani,¹⁷ M. Aguilar-Benitez,²⁷ S. Ahlen,¹² J. Alcaraz,²⁷ G. Alemani,²³ J. Allaby,¹⁸ A. Aloisio,³⁰ M.G. Alviggi,³⁰ G. Ambrosi,²⁰ H. Anderhub,⁴⁹ V.P. Andreev,^{7,38} T. Angelescu,¹⁴ F. Anselmo,¹⁰ A. Arefiev,²⁹ T. Azemoon,³ T. Aziz,¹¹ P. Bagnaia,³⁷ L. Baksay,⁴⁴ S. Banerjee,¹¹ Sw. Banerjee,¹¹ K. Banicz,⁴⁶ A. Barczyk,^{49,47} R. Barillere,¹⁸ L. Barone,³⁷ P. Bartalini,²³ A. Baschirotto,²⁸ M. Basile,¹⁰ R. Battiston,³⁴ A. Bay,²³ F. Becattini,¹⁷ U. Becker,¹⁶ F. Behner,⁴⁹ J. Berdugo,²⁷ P. Berges,¹⁶ B. Bertucci,³⁴ B.L. Betev,⁴⁹ S. Bhattacharya,¹¹ M. Biasini,³⁴ A. Biland,⁴⁹ G.M. Bilei,³⁴ J.J. Blaising,⁴ S.C. Blyth,³⁵ G.J. Bobbink,² R. Bock,¹ A. Böhm,¹ L. Boldizar,¹⁵ B. Borgia,^{18,37} D. Bourilkov,⁴⁹ M. Bourquin,²⁰ S. Braccini,²⁰ J.G. Branson,⁴⁰ V. Brigljevic,⁴⁹ I.C. Brock,³⁵ A. Buffini,¹⁷ A. Buijs,⁴⁵ J.D. Burger,¹⁶ W.J. Burger,³⁴ J. Busenitz,⁴⁴ A. Button,³ X.D. Cai,¹⁶ M. Campanelli,⁴⁹ M. Capell,¹⁶ G. Cara Romeo,¹⁰ G. Carlino,³⁰ A.M. Cartacci,¹⁷ J. Casaus,²⁷ G. Castellini,¹⁷ F. Cavallari,³⁷ N. Cavallo,³⁰ C. Cecchi,²⁰ M. Cerrada,²⁷ F. Cesaroni,²⁴ M. Chamizo,²⁷ Y.H. Chang,⁵¹ U.K. Chaturvedi,¹⁹ M. Chemarin,²⁶ A. Chen,⁵¹ G. Chen,⁸ G.M. Chen,⁸ H.F. Chen,²¹ H.S. Chen,⁸ X. Chereau,⁴ G. Chiefari,³⁰ C.Y. Chien,⁵ L. Cifarelli,³⁹ F. Cindolo,¹⁰ C. Civinini,¹⁷ I. Clare,¹⁶ R. Clare,¹⁶ G. Coignet,⁴ A.P. Colijn,² N. Colino,²⁷ S. Costantini,⁹ F. Cotoroba,¹⁴ B. de la Cruz,²⁷ A. Csilling,¹⁵ T.S. Dai,¹⁶ R.D' Alessandro,¹⁷ R. de Asmundis,³⁰ A. Degré,⁴ K. Deiters,⁴⁷ D. della Volpe,³⁰ P. Denes,³⁶ F. DeNotaristefani,³⁷ M. Diemoz,³⁷ D. van Dierendonck,² F. Di Lodovico,⁴⁹ C. Dionisi,^{18,37} M. Dittmar,⁴⁹ A. Dominguez,⁴⁰ A. Doria,³⁰ M.T. Dova,^{9,‡} D. Duchesneau,⁴ P. Duinker,² I. Duran,⁴¹ S. Easo,³⁴ H. El Mamouni,²⁶ A. Engler,³⁵ F.J. Eppling,¹⁶ F.C. Erné,² P. Extermann,²⁰ M. Fabre,⁴⁷ R. Faccini,³⁷ M.A. Falagan,²⁷ S. Falciano,³⁷ A. Favara,¹⁷ J. Fay,²⁶ O. Fedin,³⁸ M. Felcini,⁴⁹ T. Ferguson,³⁵ F. Ferroni,³⁷ H. Fesefeldt,¹ E. Fiandrini,³⁴ J.H. Field,²⁰ F. Filthaut,¹⁸ P.H. Fisher,¹⁶ I. Fisk,⁴⁰ G. Forconi,¹⁶ L. Fredj,²⁰ K. Freudenreich,⁴⁹ C. Furetta,²⁸ Yu. Galaktionov,^{29,16} S.N. Ganguli,¹¹ P. Garcia-Abia,⁶ M. Gataullin,³³ S.S. Gau,¹³ S. Gentile,³⁷ N. Gheordanescu,¹⁴ S. Giagu,³⁷ S. Goldfarb,²³ J. Goldstein,¹² Z.F. Gong,²¹ A. Gougas,⁵ G. Gratta,³³ M.W. Gruenewald,⁹ R. van Gulik,² V.K. Gupta,³⁶ A. Gurtu,¹¹ L.J. Gutay,⁴⁶ D. Haas,⁶ B. Hartmann,¹ A. Hasan,³¹ D. Hatzifotiadou,¹⁰ T. Hebbeker,⁹ A. Hervé,¹⁸ P. Hidas,¹⁵ J. Hirschfelder,³⁵ W.C. van Hoek,³² H. Hofer,⁴⁹ H. Hoorani,³⁵ S.R. Hou,⁵¹ G. Hu,⁵ I. Iashvili,⁴⁸ B.N. Jin,⁸ L.W. Jones,³ P. de Jong,¹⁸ I. Josa-Mutuberria,²⁷ R.A. Khan,¹⁹ D. Kamrad,⁴⁸ J.S. Kapustinsky,²⁵ M. Kaur,^{19,♦} M.N. Kienzle-Focacci,²⁰ D. Kim,³⁷ D.H. Kim,⁴³ J.K. Kim,⁴³ S.C. Kim,⁴³ W.W. Kinnison,²⁵ A. Kirkby,³³ D. Kirkby,³³ J. Kirkby,¹⁸ D. Kiss,¹⁵ W. Kittel,³² A. Klimentov,^{16,29} A.C. König,³² A. Kopp,⁴⁸ I. Korolko,²⁹ V. Koutsenko,^{16,29} R.W. Kraemer,³⁵ W. Krenz,¹ A. Kunin,^{16,29} P. Lacentre,^{48,‡,‡} P. Ladron de Guevara,²⁷ I. Laktineh,²⁶ G. Landi,¹⁷ C. Lapointe,¹⁶ K. Lassila-Perini,⁴⁹ P. Laurikainen,²² A. Lavorato,³⁹ M. Lebeau,¹⁸ A. Lebedev,¹⁶ P. Lebrun,²⁶ P. Lecomte,⁴⁹ P. Lecoq,¹⁸ P. Le Coultre,⁴⁹ H.J. Lee,⁹ J.M. Le Goff,¹⁸ R. Leiste,⁴⁸ E. Leonardi,³⁷ P. Levchenko,³⁸ C.Li,²¹ C.H. Lin,⁵¹ W.T. Lin,⁵¹ F.L. Linde,^{2,18} L. Lista,³⁰ Z.A. Liu,⁸ W. Lohmann,⁴⁸ E. Longo,³⁷ W. Lu,³³ Y.S. Lu,⁸ K. Lübelmeyer,¹ C. Luci,^{18,37} D. Luckey,¹⁶ L. Luminari,³⁷ W. Lustermaan,⁴⁹ W.G. Ma,²¹ M. Maity,¹¹ G. Majumder,¹¹ L. Malgeri,¹⁸ A. Malinin,²⁹ C. Mañá,²⁷ D. Mangeol,³² P. Marchesini,⁴⁹ G. Marian,^{44,¶} A. Marin,¹² J.P. Martin,²⁶ F. Marzano,³⁷ G.G. G. Massaro,² K. Mazumdar,¹¹ R.R. McNeil,⁷ S. Mele,¹⁸ L. Merola,³⁰ M. Meschini,¹⁷ W.J. Metzger,³² M. von der Mey,¹ D. Miganj,¹⁰ A. Mihul,¹⁴ A.J.W. van Mil,³² H. Milcent,¹⁸ G. Mirabelli,³⁷ J. Mnich,¹⁸ P. Molnar,⁹ B. Monteleoni,¹⁷ R. Moore,³ T. Moulík,¹¹ R. Mount,³³ G.S. Muanza,²⁶ F. Muheim,²⁰ A.J.M. Muijs,² S. Nahn,¹⁶ M. Napolitano,³⁰ F. Nessi-Tedaldi,⁴⁹ H. Newman,³³ T. Niessen,¹ A. Nippe,²³ A. Nisati,³⁷ H. Nowak,⁴⁸ Y.D. Oh,⁴³ G. Organtini,³⁷ R. Ostonen,²² S. Palit,¹³ C. Palomares,²⁷ D. Pandoulas,¹ S. Paoletti,^{37,18} P. Paolucci,³⁰ H.K. Park,³⁵ I.H. Park,⁴³ G. Pascale,³⁷ G. Passaleva,¹⁸ S. Patricelli,³⁰ T. Paul,¹³ M. Pauluzzi,³⁴ C. Paus,¹⁸ F. Pauss,⁴⁹ D. Peach,¹⁸ M. Pedace,³⁷ Y.J. Pei,¹ S. Pensotti,²⁸ D. Perret-Gallix,⁴ B. Petersen,³² S. Petrak,⁹ A. Pevsner,⁵ D. Piccolo,³⁰ M. Pieri,¹⁷ P.A. Piroué,³⁶ E. Pistolesi,²⁸ V. Plyaskin,²⁹ M. Pohl,⁴⁹ V. Pojidaev,^{29,17} H. Postema,¹⁶ J. Potier,¹⁸ N. Produit,²⁰ D. Prokofiev,³⁸ J. Quartieri,³⁹ G. Rahal-Callot,⁴⁹ N. Raja,¹¹ P.G. Rancoita,²⁸ M. Rattaggi,²⁸ G. Raven,⁴⁰ P. Razis,³¹ D. Ren,⁴⁹ M. Rescigno,³⁷ S. Reucroft,¹³ T. van Rhee,⁴⁵ S. Riemann,⁴⁸ K. Riles,³ A. Robohm,⁴⁹ J. Rodin,⁴⁴ B.P. Roe,³ L. Romero,²⁷ S. Rosier-Lees,⁴ S. Roth,¹ J.A. Rubio,¹⁸ D. Ruschmeier,⁹ H. Rykaczewski,⁴⁹ S. Sakar,³⁷ J. Salicio,¹⁸ E. Sanchez,²⁷ M.P. Sanders,³² M.E. Sarakinos,²² C. Schäfer,¹ V. Schegelsky,³⁸ S. Schmidt-Kaerst,¹ D. Schmitz,¹ N. Scholz,⁴⁹ H. Schopper,⁵⁰ D.J. Schotanus,³² J. Schwenke,¹ G. Schwering,¹ C. Sciacca,³⁰ D. Sciarrino,²⁰ L. Servoli,³⁴ S. Shevchenko,³³ N. Shivarov,⁴² V. Shoutko,²⁹ J. Shukla,²⁵ E. Shumilov,²⁹ A. Shvorob,³³ T. Siedenburg,¹ D. Son,⁴³ B. Smith,¹⁶ P. Spillantini,¹⁷ M. Steuer,¹⁶ D.P. Stickland,³⁶ A. Stone,⁷ H. Stone,³⁶ B. Stoyanov,⁴² A. Straessner,¹ K. Sudhakar,¹¹ G. Sultanov,¹⁹ L.Z. Sun,²¹ G.F. Susinno,²⁰ H. Suter,⁴⁹ J.D. Swain,¹⁹ X.W. Tang,⁸ L. Tauscher,⁶ L. Taylor,¹³ C. Timmermans,³² Samuel C.C. Ting,¹⁶ S.M. Ting,¹⁶ S.C. Tonwar,¹¹ J. Tóth,¹⁵ C. Tully,³⁶ K.L. Tung,⁸ Y. Uchida,¹⁶ J. Ulbricht,⁴⁹ E. Valente,³⁷ G. Vesztegombi,¹⁵ I. Vetlitsky,²⁹ G. Viertel,⁴⁹ M. Vivargent,⁴ S. Vlachos,⁶ H. Vogel,³⁵ H. Vogt,⁴⁸ I. Vorobiev,^{18,29} A.A. Vorobyov,³⁸ A. Vorvolakos,³¹ M. Wadhwa,⁷ W. Wallraff,¹ J.C. Wang,¹⁶ X.L. Wang,²¹ Z.M. Wang,²¹ A. Weber,¹ S.X. Wu,¹⁶ S. Wynhoff,¹ J. Xu,¹² Z.Z. Xu,²¹ B.Z. Yang,²¹ C.G. Yang,⁸ H.J. Yang,⁸ M. Yang,⁸ J.B. Ye,²¹ S.C. Yeh,⁵² J.M. You,³⁵ An. Zalite,³⁸ Yu. Zalite,³⁸ P. Zemp,⁴⁹ Y. Zeng,¹ Z.P. Zhang,²¹ B. Zhou,¹² G.Y. Zhu,⁸ R.Y. Zhu,³³ A. Zichichi,^{10,18,19} F. Ziegler,⁴⁸ G. Zilizi,^{44,¶}

- 1 I. Physikalisches Institut, RWTH, D-52056 Aachen, FRG[§]
III. Physikalisches Institut, RWTH, D-52056 Aachen, FRG[§]
 - 2 National Institute for High Energy Physics, NIKHEF, and University of Amsterdam, NL-1009 DB Amsterdam, The Netherlands
 - 3 University of Michigan, Ann Arbor, MI 48109, USA
 - 4 Laboratoire d'Annecy-le-Vieux de Physique des Particules, LAPP, IN2P3-CNRS, BP 110, F-74941 Annecy-le-Vieux CEDEX, France
 - 5 Johns Hopkins University, Baltimore, MD 21218, USA
 - 6 Institute of Physics, University of Basel, CH-4056 Basel, Switzerland
 - 7 Louisiana State University, Baton Rouge, LA 70803, USA
 - 8 Institute of High Energy Physics, IHEP, 100039 Beijing, China[△]
 - 9 Humboldt University, D-10099 Berlin, FRG[§]
 - 10 University of Bologna and INFN-Sezione di Bologna, I-40126 Bologna, Italy
 - 11 Tata Institute of Fundamental Research, Bombay 400 005, India
 - 12 Boston University, Boston, MA 02215, USA
 - 13 Northeastern University, Boston, MA 02115, USA
 - 14 Institute of Atomic Physics and University of Bucharest, R-76900 Bucharest, Romania
 - 15 Central Research Institute for Physics of the Hungarian Academy of Sciences, H-1525 Budapest 114, Hungary[‡]
 - 16 Massachusetts Institute of Technology, Cambridge, MA 02139, USA
 - 17 INFN Sezione di Firenze and University of Florence, I-50125 Florence, Italy
 - 18 European Laboratory for Particle Physics, CERN, CH-1211 Geneva 23, Switzerland
 - 19 World Laboratory, FBLJA Project, CH-1211 Geneva 23, Switzerland
 - 20 University of Geneva, CH-1211 Geneva 4, Switzerland
 - 21 Chinese University of Science and Technology, USTC, Hefei, Anhui 230 029, China[△]
 - 22 SEFT, Research Institute for High Energy Physics, P.O. Box 9, SF-00014 Helsinki, Finland
 - 23 University of Lausanne, CH-1015 Lausanne, Switzerland
 - 24 INFN-Sezione di Lecce and Università Degli Studi di Lecce, I-73100 Lecce, Italy
 - 25 Los Alamos National Laboratory, Los Alamos, NM 87544, USA
 - 26 Institut de Physique Nucléaire de Lyon, IN2P3-CNRS, Université Claude Bernard, F-69622 Villeurbanne, France
 - 27 Centro de Investigaciones Energéticas, Medioambientales y Tecnológicas, CIEMAT, E-28040 Madrid, Spain[‡]
 - 28 INFN-Sezione di Milano, I-20133 Milan, Italy
 - 29 Institute of Theoretical and Experimental Physics, ITEP, Moscow, Russia
 - 30 INFN-Sezione di Napoli and University of Naples, I-80125 Naples, Italy
 - 31 Department of Natural Sciences, University of Cyprus, Nicosia, Cyprus
 - 32 University of Nijmegen and NIKHEF, NL-6525 ED Nijmegen, The Netherlands
 - 33 California Institute of Technology, Pasadena, CA 91125, USA
 - 34 INFN-Sezione di Perugia and Università Degli Studi di Perugia, I-06100 Perugia, Italy
 - 35 Carnegie Mellon University, Pittsburgh, PA 15213, USA
 - 36 Princeton University, Princeton, NJ 08544, USA
 - 37 INFN-Sezione di Roma and University of Rome, "La Sapienza", I-00185 Rome, Italy
 - 38 Nuclear Physics Institute, St. Petersburg, Russia
 - 39 University and INFN, Salerno, I-84100 Salerno, Italy
 - 40 University of California, San Diego, CA 92093, USA
 - 41 Dept. de Física de Partículas Elementales, Univ. de Santiago, E-15706 Santiago de Compostela, Spain
 - 42 Bulgarian Academy of Sciences, Central Lab. of Mechatronics and Instrumentation, BU-1113 Sofia, Bulgaria
 - 43 Center for High Energy Physics, Adv. Inst. of Sciences and Technology, 305-701 Taejeon, Republic of Korea
 - 44 University of Alabama, Tuscaloosa, AL 35486, USA
 - 45 Utrecht University and NIKHEF, NL-3584 CB Utrecht, The Netherlands
 - 46 Purdue University, West Lafayette, IN 47907, USA
 - 47 Paul Scherrer Institut, PSI, CH-5232 Villigen, Switzerland
 - 48 DESY-Institut für Hochenergiephysik, D-15738 Zeuthen, FRG
 - 49 Eidgenössische Technische Hochschule, ETH Zürich, CH-8093 Zürich, Switzerland
 - 50 University of Hamburg, D-22761 Hamburg, FRG
 - 51 National Central University, Chung-Li, Taiwan, China
 - 52 Department of Physics, National Tsing Hua University, Taiwan, China
- [§] Supported by the German Bundesministerium für Bildung, Wissenschaft, Forschung und Technologie
[‡] Supported by the Hungarian OTKA fund under contract numbers T019181, F023259 and T024011.
[¶] Also supported by the Hungarian OTKA fund under contract numbers T22238 and T026178.
[‡] Supported also by the Comisión Interministerial de Ciencia y Tecnología.
[‡] Also supported by CONICET and Universidad Nacional de La Plata, CC 67, 1900 La Plata, Argentina.
[‡] Supported by Deutscher Akademischer Austauschdienst.
[◇] Also supported by Panjab University, Chandigarh-160014, India.
[△] Supported by the National Natural Science Foundation of China.

Selection of Process	Efficiencies [%] for									
	$e\nu e\nu$	$e\nu\mu\nu$	$e\nu\tau\nu$	$\mu\nu\mu\nu$	$\mu\nu\tau\nu$	$\tau\nu\tau\nu$	$qqe\nu$	$qq\mu\nu$	$qq\tau\nu$	$qqqq$
$e^+e^- \rightarrow e\nu e\nu(\gamma)$	62.1	0.1	11.0			1.9				
$e^+e^- \rightarrow e\nu\mu\nu(\gamma)$		56.5	9.0	0.1	9.1	1.1				
$e^+e^- \rightarrow e\nu\tau\nu(\gamma)$	8.0	1.4	37.6		0.3	9.3				
$e^+e^- \rightarrow \mu\nu\mu\nu(\gamma)$				45.6	6.8	0.5				
$e^+e^- \rightarrow \mu\nu\tau\nu(\gamma)$		4.1	0.5	2.7	33.2	7.7				
$e^+e^- \rightarrow \tau\nu\tau\nu(\gamma)$	0.2	0.2	3.6		1.2	22.0				
$e^+e^- \rightarrow qqe\nu(\gamma)$							85.4	0.2	2.1	
$e^+e^- \rightarrow qq\mu\nu(\gamma)$							0.1	77.0	4.3	
$e^+e^- \rightarrow qq\tau\nu(\gamma)$							4.8	6.0	50.1	0.2
$e^+e^- \rightarrow qqqq(\gamma)$							0.3		1.7	87.5

Table 1: Selection efficiencies for signal processes $e^+e^- \rightarrow l\nu l\nu(\gamma)$, $e^+e^- \rightarrow qq\ell\nu(\gamma)$, and $e^+e^- \rightarrow qqqq(\gamma)$. For the $l\nu l\nu$ ($qqe\nu$) selections, the signal efficiency is derived from a CC56+NC56 (CC20) Monte Carlo sample and is given within phase-space cuts, see Section 2.1 (2.2). For the $qqqq$ selection, the numbers are quoted for a neural-network output larger than 0.67.

Selection of Process	N_{data}	Background [pb]	Conversion Factor f
$e^+e^- \rightarrow e\nu e\nu(\gamma)$	9	0.026 ± 0.011	0.90
$e^+e^- \rightarrow e\nu\mu\nu(\gamma)$	9	0.014 ± 0.009	1.07
$e^+e^- \rightarrow e\nu\tau\nu(\gamma)$	11	0.068 ± 0.014	1.07
$e^+e^- \rightarrow \mu\nu\mu\nu(\gamma)$	8	0.002 ± 0.002	0.95
$e^+e^- \rightarrow \mu\nu\tau\nu(\gamma)$	14	0.022 ± 0.009	1.09
$e^+e^- \rightarrow \tau\nu\tau\nu(\gamma)$	3	0.043 ± 0.012	0.95
$e^+e^- \rightarrow qqe\nu(\gamma)$	112	0.120 ± 0.006	1.09
$e^+e^- \rightarrow qq\mu\nu(\gamma)$	108	0.102 ± 0.034	—
$e^+e^- \rightarrow qq\tau\nu(\gamma)$	77	0.191 ± 0.013	—
$e^+e^- \rightarrow qqqq(\gamma)$	473	1.463 ± 0.075	—

Table 2: Number of selected data events, N_{data} , and accepted background cross sections from non- W processes for the selections of the signal processes $e^+e^- \rightarrow \ell\nu\ell\nu(\gamma)$, $e^+e^- \rightarrow qq\ell\nu(\gamma)$, and $e^+e^- \rightarrow qqqq(\gamma)$. The error combines Monte Carlo statistics and systematic effects in quadrature. For the $qqqq$ selection, the numbers are quoted for a neural-network output larger than 0.67. The ratio of the CC03 cross section without cuts and the four-fermion cross section within phase-space cuts is calculated with EXCALIBUR and listed in the last column.

Systematic Errors on σ [%]					
Source	Final State				
	$\ell\nu\ell\nu$	$qqe\nu$	$qq\mu\nu$	$qq\tau\nu$	$qqqq$
MC statistics signal	0.7	0.3	0.3	0.5	0.1
Selection systematics	1.0	1.3	1.2	2.6	1.5
MC statistics background	3.0	0.2	0.7	1.4	0.2
Background systematics	—	0.2	0.3	0.3	1.0
ISR simulation	0.4	0.2	0.1	0.1	0.1
FSR simulation	0.6	0.6	0.8	0.4	—
W mass (± 0.25 GeV)	0.1	0.3	0.2	0.3	0.3
W width (± 0.50 GeV)	0.4	0.3	0.3	0.5	0.6
Colour Reconnection	—	—	—	—	0.6
Bose-Einstein effects	—	0.6	0.1	1.1	1.3
Fragmentation and Decay	—	0.2	0.2	0.2	1.0
CC03 versus 4F	—	—	0.2	0.2	0.6
Total	3.3	1.7	1.7	3.3	2.7

Table 3: Contributions to the systematic error in the cross section measurements. The systematic uncertainties are relative to the cross sections listed in Table 4.

Process	N_{data}	N_{bg}	$\sigma(\text{CC03})$ [pb]	σ_{SM} [pb]	r_{SM} [%]
$e^+e^- \rightarrow \ell\nu\ell\nu(\gamma)$	54	9.7	$1.49 \pm 0.25 \pm 0.05$	1.67	10.6
$e^+e^- \rightarrow qqe\nu(\gamma)$	112	6.7	$2.36 \pm 0.24 \pm 0.04$	2.29	14.6
$e^+e^- \rightarrow qq\mu\nu(\gamma)$	108	5.7	$2.29 \pm 0.24 \pm 0.04$	2.29	14.6
$e^+e^- \rightarrow qq\tau\nu(\gamma)$	77	10.6	$1.86 \pm 0.32 \pm 0.06$	2.29	14.6
$e^+e^- \rightarrow qqqq(\gamma)$	473	81.2	$8.35 \pm 0.46 \pm 0.23$	7.17	45.6

Table 4: Number of selected data events, N_{data} , number of expected non-W background events, N_{bg} , and CC03 cross sections for the reactions $e^+e^- \rightarrow qqe\nu(\gamma)$, $e^+e^- \rightarrow qq\mu\nu(\gamma)$, $e^+e^- \rightarrow qq\tau\nu(\gamma)$, $e^+e^- \rightarrow \ell\nu\ell\nu(\gamma)$ and $e^+e^- \rightarrow qqqq(\gamma)$. For the $qqqq$ signal, the numbers N_{data} and N_{bg} correspond to a cut on the output of the neural network at 0.67, while the $qqqq$ cross section is obtained from a fit to the neural-network output distribution as described in Section 2.5. The first error is statistical and the second systematic. Also shown are the CC03 cross sections, σ_{SM} , and the CC03 ratios, r_{SM} , as expected within the Standard Model.

Parameter	Lepton Non-Universality	Lepton Universality	Standard Model
$B(W \rightarrow e\nu)$ [%]	$10.5 \pm 0.9 \pm 0.2$	—	
$B(W \rightarrow \mu\nu)$ [%]	$10.2 \pm 0.9 \pm 0.2$	—	
$B(W \rightarrow \tau\nu)$ [%]	$9.0 \pm 1.2 \pm 0.3$	—	
$B(W \rightarrow \ell\nu)$ [%]	—	$10.0 \pm 0.4 \pm 0.1$	10.8
$B(W \rightarrow qq)$ [%]	$70.4 \pm 1.3 \pm 0.4$	$70.1 \pm 1.3 \pm 0.4$	67.5
σ_{WW} [pb]	$16.34 \pm 0.67 \pm 0.26$	$16.45 \pm 0.67 \pm 0.26$	15.72

Table 5: W-decay branching fractions, B , and total W-pair cross section, σ_{WW} , derived with and without the assumption of charged-current lepton universality. The correlations between the leptonic branching fractions are -0.03 , -0.27 , -0.29 for $(e\mu)$, $(e\tau)$, $(\mu\tau)$, respectively. Also shown are the W-decay branching fractions [3] and the total W-pair cross section as expected in the Standard Model.

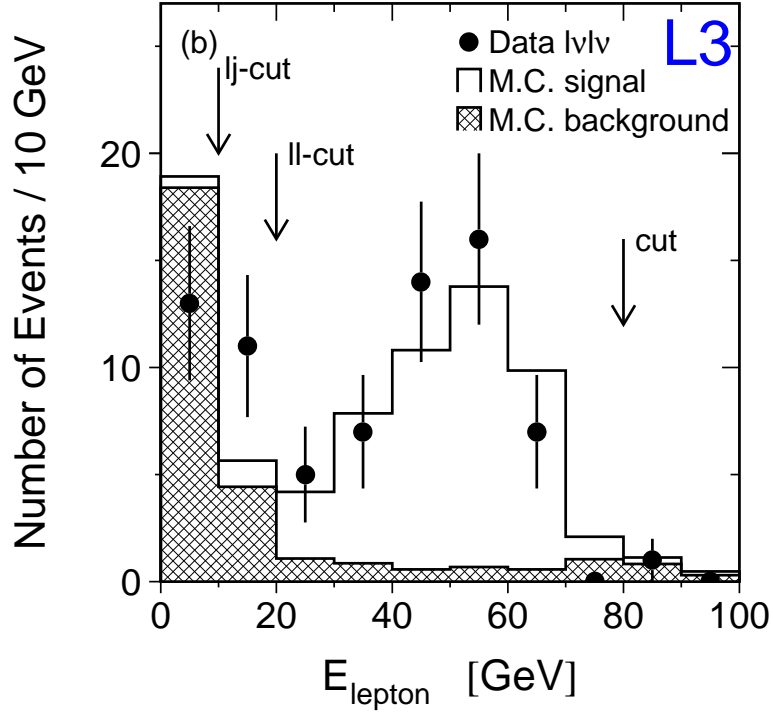
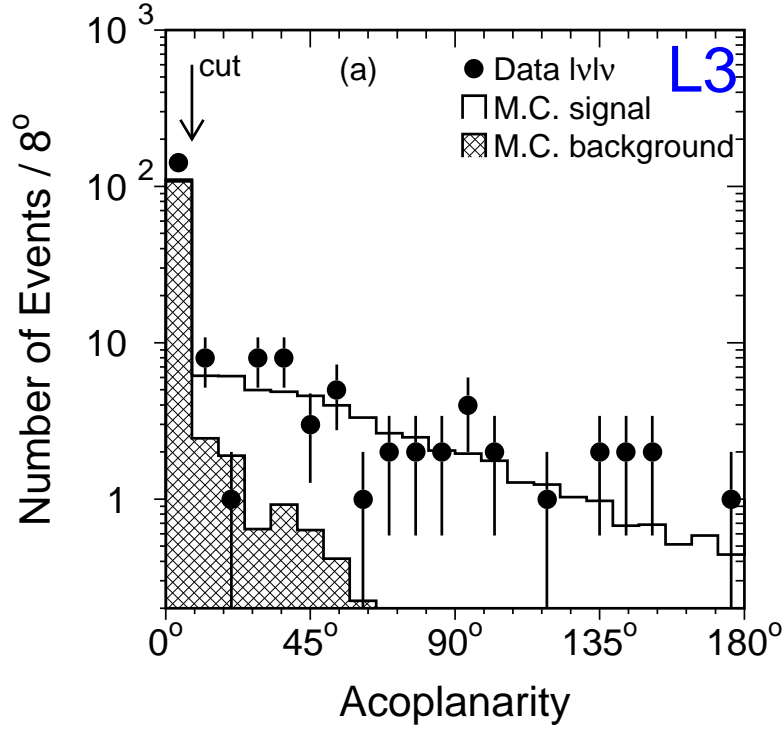


Figure 1: Distributions of variables used for the selection of $e^+e^- \rightarrow \ell\nu\ell\nu(\gamma)$ events, adding the lepton-lepton (ll) and lepton-jet (lj) classes, comparing the signal and background Monte Carlo to the data. The position of the selection cuts are indicated by vertical arrows, see text. All selection cuts except in the variable plotted are applied. (a) The acoplanarity between the two leptons or the lepton and the jet. (b) The energy of the identified electron or muon with highest energy, E_{lepton} .

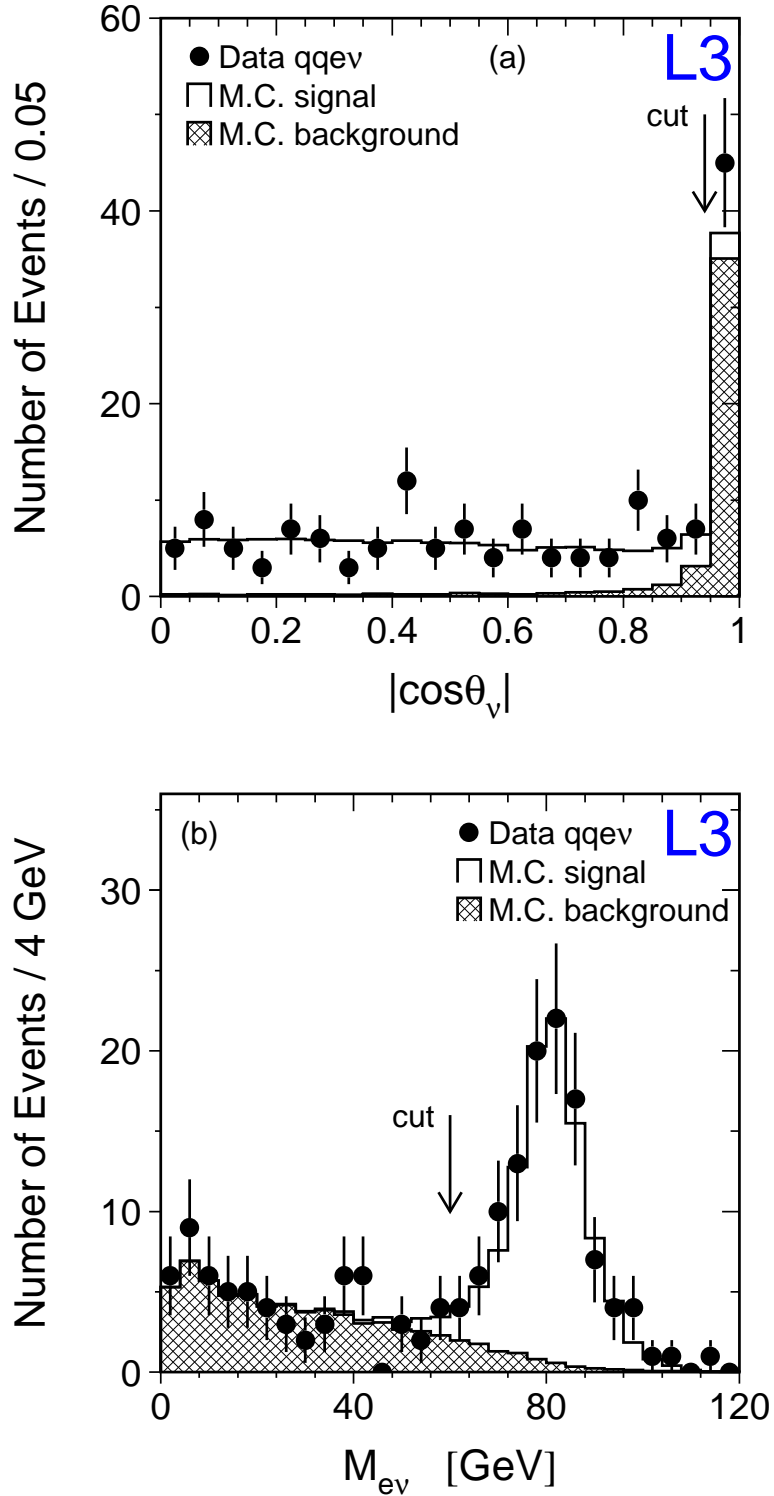


Figure 2: Distributions of variables used for the selection of $e^+e^- \rightarrow qqe\nu(\gamma)$ events with the electron identified in the BGO electromagnetic calorimeter. (a) The polar angle of the neutrino, $|\cos\theta_\nu|$. (b) The invariant mass of the electron-neutrino system, $M_{e\nu}$.

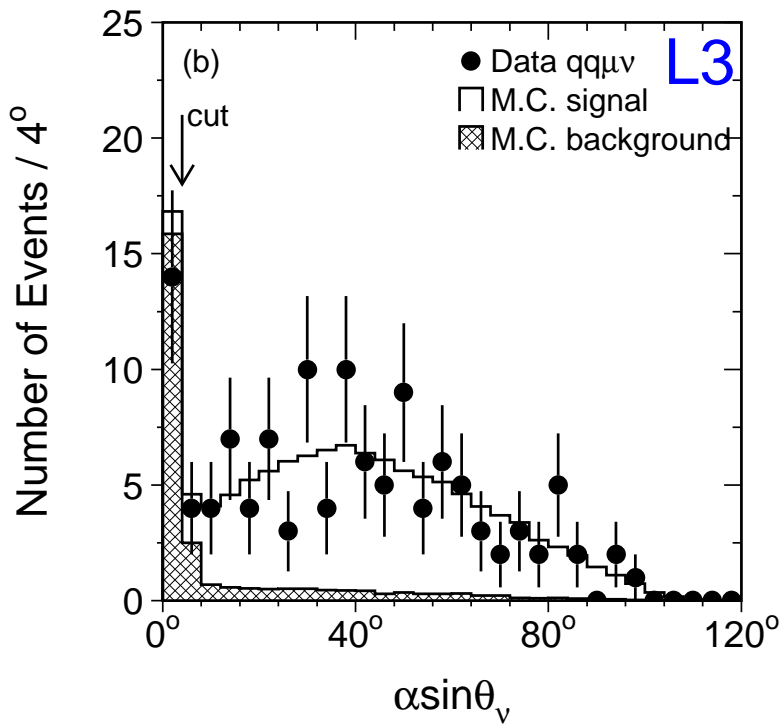
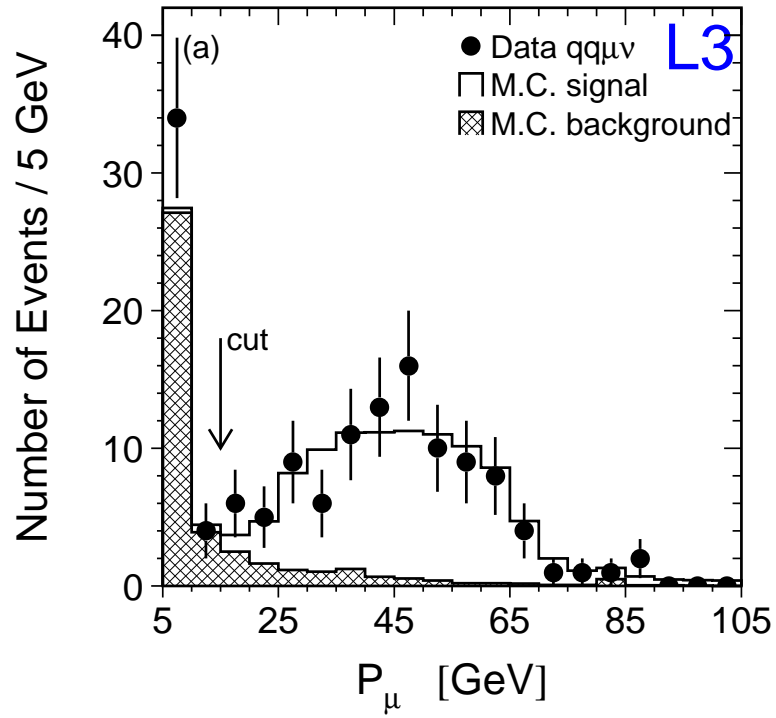


Figure 3: Distributions of variables used for the selection of $e^+e^- \rightarrow qq\mu\nu(\gamma)$ events. (a) The muon momentum, P_μ . (b) The quantity $\alpha \sin \theta_\nu$ defined in the text.

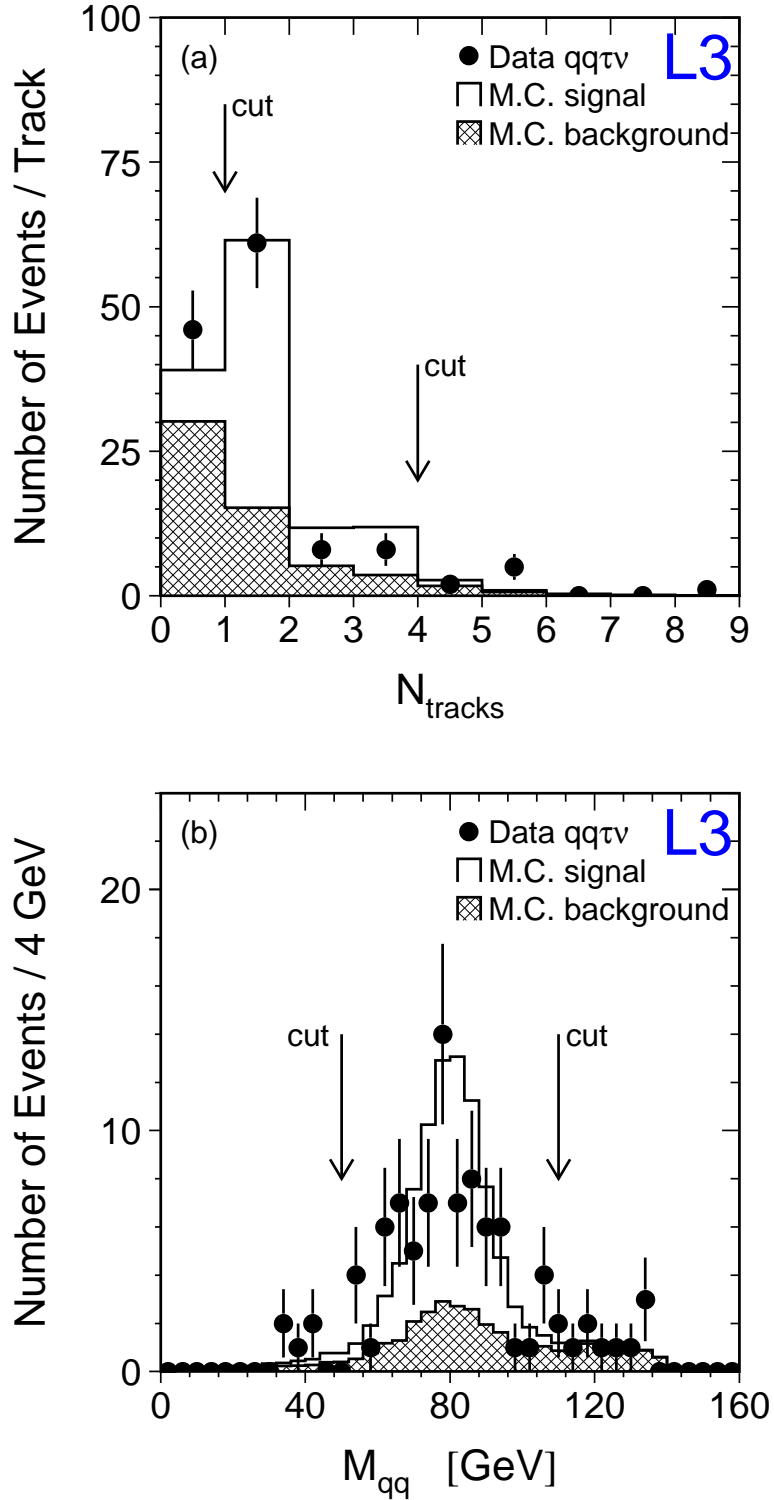


Figure 4: Distributions of variables used for the selection of $e^+e^- \rightarrow qq\tau\nu(\gamma)$ events. (a) The number of TEC tracks associated to the τ jet, N_{tracks} . (b) The invariant mass of the jet-jet system, M_{qq} .

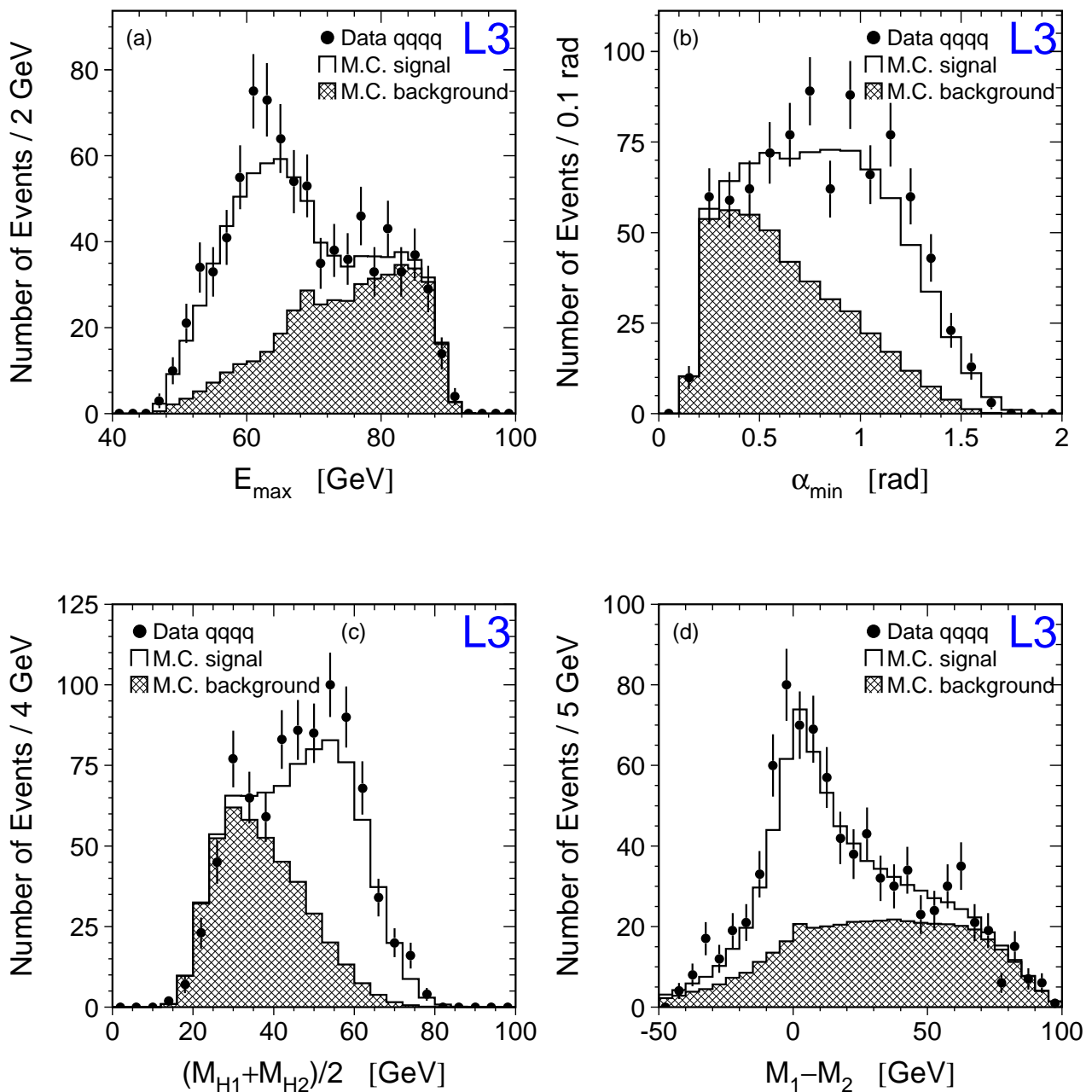


Figure 5: Distributions of variables used for the neural network in the analysis of $e^+e^- \rightarrow qqqq(\gamma)$ events. All selection cuts are applied. (a) The maximal jet energy, E_{\max} . (b) The minimal jet-jet opening angle, α_{\min} . (c) The average mass of the two jets when the event is reconstructed as a two-jet event, $(M_{H1} + M_{H2})/2$. (d) The difference of the two W masses, $M_1 - M_2$, where the first W contains the jet with highest energy.

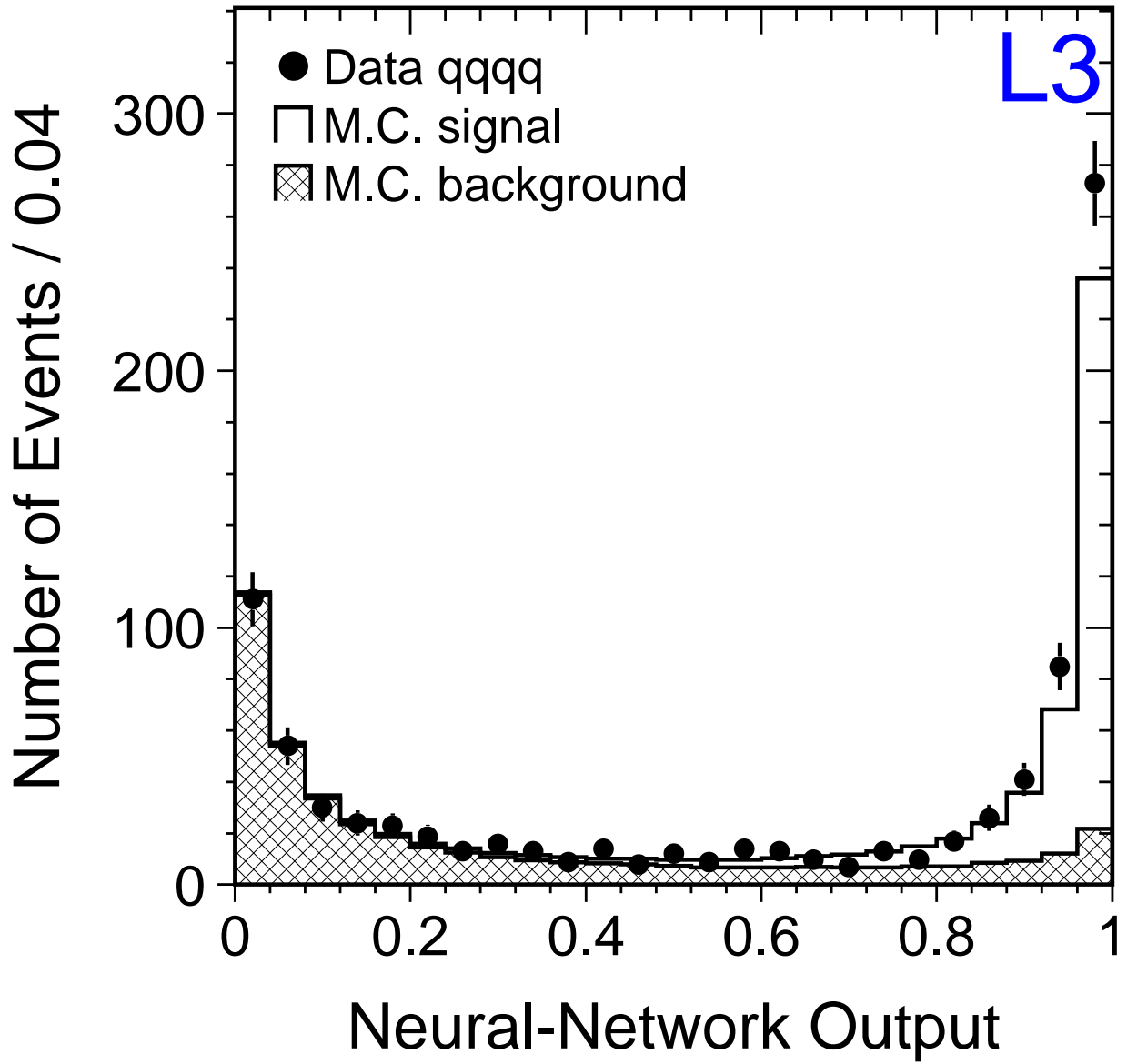


Figure 6: Distribution of the output of the neural network used in the analysis of $e^+e^- \rightarrow qqqq(\gamma)$ events.

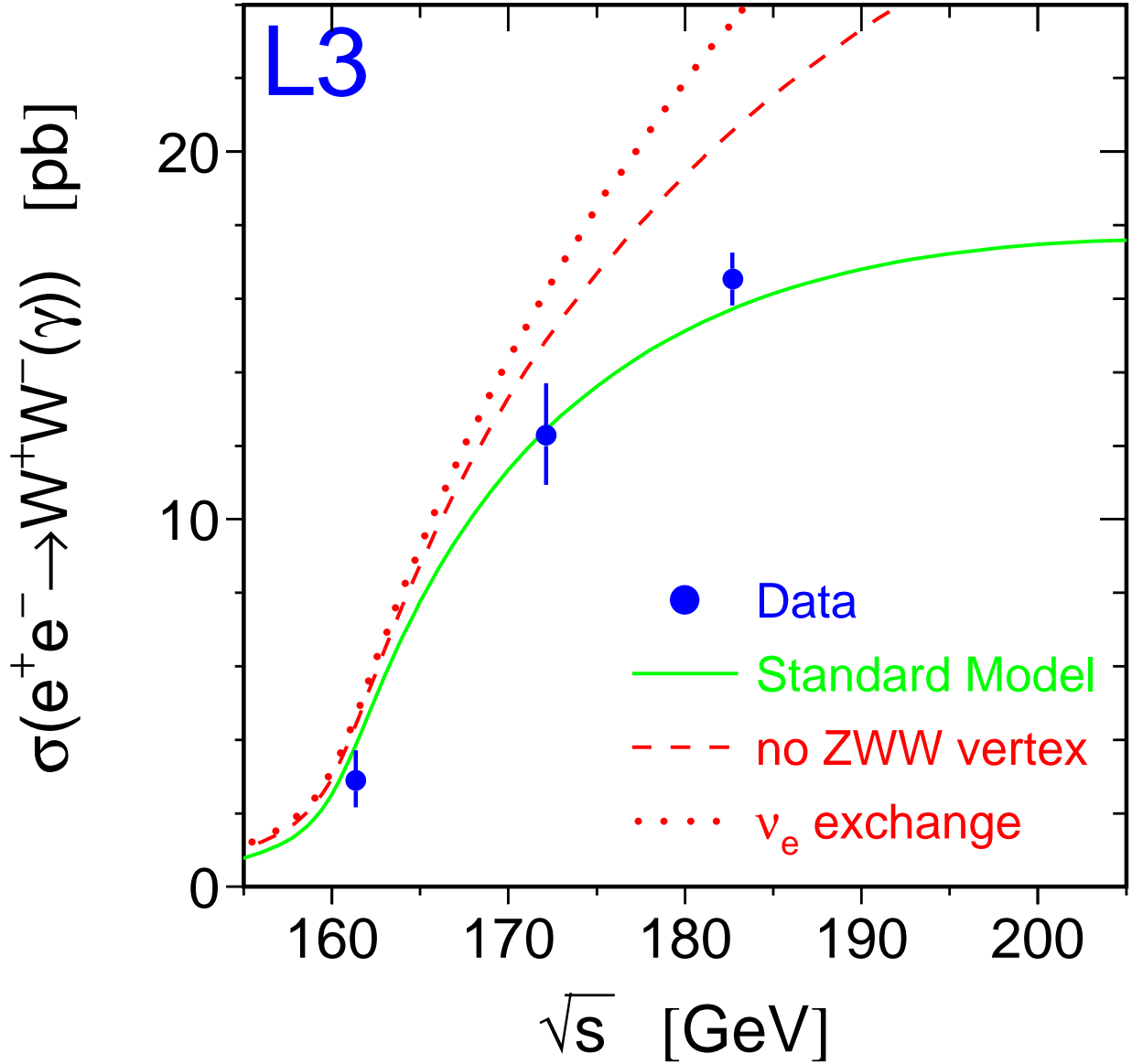


Figure 7: The cross section, σ_{WW} , of the process $e^+e^- \rightarrow WW \rightarrow ffff(\gamma)$ as a function of the centre-of-mass energy, \sqrt{s} . The published measurements of σ_{WW} at $\sqrt{s} = 161$ GeV and at $\sqrt{s} = 172$ GeV, and the new measurement at $\sqrt{s} = 183$ GeV are shown as dots with error bars, combining statistical and systematic errors in quadrature. The solid curve shows the Standard Model expectation. The dashed curve shows the expectation if there is no ZWW coupling. The dotted curve shows the expectation if only t -channel ν_e exchange in W-pair production is considered.